RSC Advances

PAPER

View Article Online
View Journal | View Issue

Cite this: *RSC Adv.*, 2021, **11**, 26700

Enhanced capacitive performance of cathodically reduced titania nanotubes pulsed deposited with Mn_2O_3 as supercapacitor electrode

Muhammad Muhammad Muzakir,[ab] Zulkarnain Zainal,*[ac] Hong Ngee Lim,[ac] Abdul Halim Abdullah[ac] and Noor Nazihah Bahrudin[a]

A facile and simple pulse electrodeposition method was employed to deposit Mn_2O_3 nanoparticles on cathodically reduced titania nanotubes (R-TNTs) at different deposition time in the range of 3–15 min to investigate the influence of mass loading of Mn_2O_3 on the electrochemical performance of Mn_2O_3/R-TNTs nanocomposite for supercapacitor application. Mn_2O_3 nanoparticles were deposited on circumference of R-TNTs as well as in the nanotubes as revealed by FESEM images for all the deposited time. XPS result confirmed the presence of MnO_2 (Mn^{4+}) and MnO (Mn^{2+}) on the Mn_2O_3/R-TNTs composite which provide pseudocapacitive behaviour for the electrode. Mass loading of Mn_2O_3 increased linearly with deposition time as confirmed by EDX analysis. The sample deposited for 12 min exhibits the highest areal capacitance of 51 mF cm^{-2} (which is 22 times enhancement over R-TNTs) at a current density of 0.1 mA cm^{-2} and specific capacitance of 325 F g^{-1} at 6 A g^{-1}. The sample also show a high-rate capability by retaining 80% of its capacitance even at higher current density of 30 A g^{-1}. Interestingly, it retained 98% of the capacitance over 5000 charge discharge cycles at 10 A g^{-1} after initial drop to 95% at 200th cycles suggesting an excellent long-term chemical stability. A considerably low equivalent series resistance (ESR) and charge transfer resistance (R_{ct}) of 9.6 Ω and 0.4 Ω respectively was deduced from electrochemical impedance spectroscopy (EIS) analysis indicating good conductivity and improved charge transfer efficiency of Mn_2O_3/R-TNTs nanocomposite.

Received 22nd January 2021
Accepted 4th July 2021

DOI: 10.1039/d1ra00564b

rsc.li/rsc-advances

Introduction

There is a rapidly increasing demand for energy conversion and storage devices such as supercapacitors, batteries, and fuel cells due to environmental issues posed by fossil fuels and the appearance of serious energy crisis.[1,2] Supercapacitors have attracted a wide research attention because of their unique properties, such as fast charge–discharge rates and longer cycle life than batteries, and higher energy density than conventional capacitors. Based on their charge–discharge mechanism, supercapacitors can be majorly categorised into electrochemical double layer capacitors (EDLCs) in which charge storage occurs at the electrode–electrolyte interface and pseudocapacitors where charge storage occurs *via* fast and reversible surface reactions.[3–5] In general, carbon-based materials such as graphene, activated carbon, carbon nanotubes (CNTs), are the most employed electrode material in EDLCs whereas metal oxides such as MnO_2, RuO_2, NiO, Fe_3O_4, Co_3O_2, SnO_2 are the frequently used materials in pseudocapacitors.[6–14]

Among the pseudocapacitive material, MnO_2 has attracted a great deal of attention because of its low cost, availability, wide electrochemical potential window, environmentally-friendly and high theoretical capacitance value (1370 F g^{-1}).[5,15,16] However, the practical capacitance value of MnO_2 has deviated far from the theoretical value because of its poor electrical conductivity of 10^{-5} to 10^{-6} S cm^{-1} and densely packed nonporous structure.[17,18] To over-come this drawback, considerable efforts were devoted to synthesised nanoscale MnO_2 and incorporate it into a more electrically conductive, stable, and highly surface area nanostructured materials such as CNTs,[19] carbon nanofibers,[20] and titania nanotubes (TNTs).[17]

Highly ordered TNTs synthesized by the electrochemical anodization method, have received great attention due to their simple fabrication method, excellent controllability, high electrical conductivity (10^{-5} to 10^{-2} S cm^{-1}), good chemical stability, and most importantly it offers an extremely large and solvated ions accessible surface area in addition to acting as a binder-free electrode as well as a substrate to support electroactive materials such as MnO_2 nanoparticles.[5,16,21]

Deposition of nanosized MnO_2 onto TNTs have numerous advantages to the electrochemical performance of the MnO_2/TNTs composite. Contrary to the planar substrate, the

---

[a] *Department of Chemistry, Faculty of Science, Universiti Putra Malaysia, Serdang, Selangor 43400, Malaysia. E-mail: zulkar@upm.edu.my; Tel: +6-03-97696810*

[b] *Department of Chemistry, Faculty of Science, Gombe State University, Gombe PMB 127, Nigeria*

[c] *Materials Synthesis and Characterization Laboratory, Institute of Advanced Technology, Universiti Putra Malaysia, Serdang, Selangor 43400, Malaysia*

nanotubular structure of TNTs offers unique properties conducive for rapid transfer of electrolytes ions during charge discharge processes in the electrode/electrolyte interface. It also provides an increased electronic and ionic sites that will enhance energy density of the MnO_2/TNTs composite.[4,5]

However, it was established that TNTs suffer from a very low areal capacitance less than 1 mF cm^{-2} due to its n-type semiconductor nature.[6] Several strategies have been employed to improve the capacitive performance of the TNTs electrode *via* thermal treatments to change the amorphous phase to anatase or rutile,[22] hydrogenation to increase the donor densities,[23] and electrochemical cathodic polarization to induced oxygen vacancies and reduced Ti^{4+} to Ti^{3+}.[24] Significant enhancement in the conductivity and capacitance of TNTs have been achieved through these various modifications which make it a suitable substrate or current collector that could serve as an easy path for fast transportation of ions and electrons, resulting in a reduced internal resistance and improved pseudocapacitive performance.[25–27] Thus, attempts on the deposition of MnO_2 onto the modified TNTs have been made by hydrothermal,[8] sonochemical,[10] and chemical bath deposition,[15,21] these methods involved intensive control conditions such as high temperatures or longer preparation time.

Electrodeposition is advantageous compared to chemical solution methods as a facile, simple, and single step method, it can control the composition and thickness of the thin film with good adhesion to the current collector. Moreover, the desired morphology can be easily controlled by adjusting the deposition parameters.[4,28] For electrodeposition of MnO_2 onto the TNTs, many studies have focused on potentiostatic (chronoamperometry), galvanostatic (chronopotentiometry) or cyclic voltammetry modes of electrodepositions.[5,19,20,29,30] However, these approaches resulted in the deposition of MnO_2 species only on the top of the TNTs and in some cases causing the deposits to cover the nanotubes openings. This leads to non-utilization of the entire surface of the nanotubes which result in low coverage and specific capacitance values.[4,31] Pulse electrodeposition (PED) is another mode of electrodeposition that is considered as a useful technique for the synthesis of novel electroactive materials.[32] Smooth, homogenous, and uniform deposits along the elongated tube walls can be obtained by this technique. The physico-chemical properties of materials (such as morphology, electrical conductivity, porosity, adhesion, and compound content) can be controlled through modifying pulse parameters.[12] Zhou *et al.*[3] reported pulse current electrodeposition of MnO_2 onto cathodically polarized TNTs with the deposit along the nanotubes wall has achieved a specific capacitance of 425 F g^{-1}. Samsudin *et al.*[13] have successfully deposited Mn_2O_3 onto reduced TNTs *via* the reverse pulse potential electrodeposition with areal capacitance of 18.32 mF cm^{-2}.

In this study, PED was employed to deposit Mn_2O_3 nanoparticles onto the R-TNTs. The influence of deposition time on the mass loading of Mn_2O_3 on R-TNTs which in turn affects the morphology and electrochemical performance of the Mn_2O_3/R-TNTs composite as electrode in supercapacitor application has been investigated. To specifically demonstrate the role of TNTs in electrochemical performance of the Mn_2O_3/R-TNTs composite, Mn_2O_3 was also deposited on the planar Ti foil without the nanotubes.

Materials and methods

Preparation of reduced titania nanotubes (R-TNTs)

Titanium foil (0.25 mm thickness, 99.7% purity, Sigma Aldrich) was cut into 1 × 1 cm^2 and cleaned by series of sonication in acetone, isopropanol and deionized (DI) water, for 15 min each followed by chemical etching in 3 M HNO_3 (65%, MERCK) for 10 min, and finally rinsed with excess DI water and dried in air. The synthesis of TNTs by anodization was conducted in two-electrode electrochemical cell with titanium foil as the anode and high-density graphite as the cathode at room temperature. The electrolyte used was a mixture of glycerol (99.8% purity, initial water content 0.03 wt%, Fisher Scientific), 0.5 wt% NH_4F (FLUKA) and 25 v/v% water. The anodization was carried out at constant voltage of 30 V for 1 h using a DC power supply (Consort Mini, Cleaver Scientific Ltd). A distance of 2 cm was maintained between the two electrodes in all the experiments. Immediately after the anodization, the samples were rinsed with DI water, dried in air, and then calcined at 500 °C under air atmosphere for 2 h at a heating rate of 2 °C min^{-1}. Electrochemical reduction of the sample was conducted in the same electrochemical cell with the anodized sample as the cathode and high-density graphite as anode in 0.5 M Na_2SO_4 solution as supporting electrolyte at constant voltage of 5 V for 30 s. The sample was rinsed with DI water and dried at room temperature.

Preparation of Mn_2O_3/R-TNTs

PED mode was used for deposition of Mn_2O_3 onto the R-TNTs. This was conducted in a three-electrode electrochemical cell by employing R-TNTs, Ag/AgCl (3 M KCl) and Pt wire as working, reference and counter electrode respectively using potentiostat–galvanostat (Autolab PGSTAT204/FRA32M module). 5 mM $MnSO_4$ containing 40 mM Na_2SO_4 was used as deposition electrolyte. Prior to the PED, cyclic voltammetry of the electrolyte was run from −1.0 V to 1.0 V to determine the deposition potential of the Mn_2O_3. In the PED, one pulse consisted of applying a cathodic potential of −0.6 V for 1 s and −0.2 V for 9 s representing 10% duty cycle. The deposition was conducted for 3, 6, 9, 12 and 15 min and finally the samples were dried in an oven at 80 °C.

Material characterization and electrochemical measurements

The morphology and microstructure of the prepared samples were examined by field emission scanning electron microscopy (FESEM, JSM-7600F, JOEL, Japan) equipped with an energy dispersive X-ray spectrometer (EDS). Phase identification and chemical states of the samples were investigated using X-ray diffraction (XRD, Shimadzu, D60000, Japan) with Cu K_α (λ = 1.5406 Å) radiation and X-ray photoelectron spectroscopy (XPS, PHI Quantera II) respectively. The electrochemical performance of the electrode was investigated by cyclic voltammetry (CV), galvanostatic charge–discharge (GCD) and EIS using a conventional three-electrode cell (Auto lab PGSTAT204/FRA32M) in 1 M KCl aqueous solution as electrolyte at room temperature. EIS was conducted at open circuit potential (OPC) in the frequency range of 0.01 Hz to 1 MHz with a perturbation amplitude of

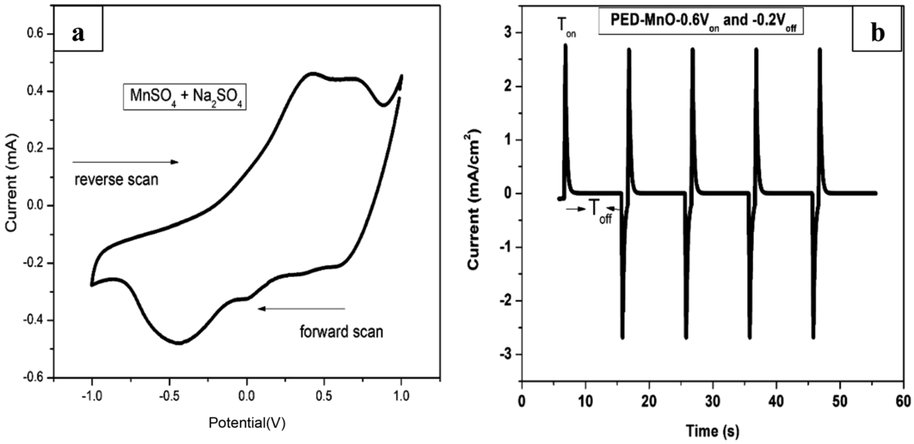

Fig. 1 (a) Cyclic voltammogram of $MnSO_4$ containing Na_2SO_4 at a scan rate of 20 mV s^{-1} (b) the output of pulse deposition graph for a few selected cycles.

5 mV. The areal capacitance (C_A) and specific capacitance (SC) of the samples was calculated based on the GCD curves using eqn (1) and (2), respectively:[4,33]

$$C_A = \frac{I\Delta t}{\Delta EA}\ \left(\mathrm{F\ cm^{-2}}\right) \tag{1}$$

$$SC = \frac{I\Delta t}{\Delta Em}\ \left(\mathrm{F\ g^{-1}}\right) \tag{2}$$

where I is the discharge current in amperes, Δt is the discharge time in seconds, ΔE is the difference in discharge voltage in volts, A is the area of the active electrode in $cm,^2$ and m is the mass of the active electrode material in gram.

Results and discussion

Fig. 1a shows a CV voltammogram for $MnSO_4$ containing Na_2SO_4 swept from −1.0 to 1.0 V at a scan rate of 20 mV s^{-1}. A broad reduction peak on the forward scan with a maximum cathodic current at around −0.5 V is associated with the deposition of Mn. Meanwhile on the reverse scan, the highest anodic peak was observed at around 0.40 V which is due to the dissolution of the Mn. Based on the cathodic reduction peak from the CV, −0.6 V was selected as the deposition potential (V_{on}) of Mn. On the other hand, the dissolution potentials (V_{off}) applied was −0.2 V which is the onset of Mn dissolution corresponding to zero current. Fig. 1b presents a few selected pulses from PED experiment.

Morphology and composition analyses

Phase identification and elemental composition of the prepared samples were investigated by XRD and XPS. Fig. 2a shows the XRD patterns of TNTs, R-TNTs, and Mn_2O_3/R-TNTs samples. Peaks at around 35.1°, 38.4°, 40.2°, 53.2°, 63.0°, 71.0°, 76.2° and 77.4° corresponding to hexagonal Ti substrate (JCPDS: 00-044-1294) and peaks at 25.7° and 48.5° which are indexed to (101) and (200) planes of pure anatase phase (JCPDS: 01-075-1537) were found in all the samples. After cathodic reduction, the XRD pattern of the R-TNTs remained the same as the calcined TNTs with slight increment in the intensity of anatase peak. No prominent peak corresponding to the Mn_2O_3 was observed which may be ascribed to the dominant peaks from the substrate (R-TNTs) which retained its crystalline phase as reported elsewhere.[15,21,27]

Mn_2O_3/R-TNTs sample was further characterized by XPS, the survey spectra of the sample depicted in Fig. 2b indicates the presence of four elements (Ti, O, Mn, C) in the sample. The Mn 2p spectra in Fig. 2c shows the presence of two spin–orbit doublets, where one pair of peaks at 640.8 and 651.9 eV are associated with $2p_{3/2}$ and $2p_{1/2}$ spectra of MnO, another pair of peaks centred at 642.2 and 653.4 eV are associated with $2p_{3/2}$, and $2p_{1/2}$ spectra of MnO_2, respectively.[15,18,30,34] This confirmed that there are two types of Mn oxidation states (Mn^{2+} & Mn^{4+}) in the sample as reported elsewhere.[35–38] The peak at around 646 eV could be assigned to MnO satellite feature.[14] To confirm the variation of oxidation state of Mn during redox reaction, the O 1s core level spectra was analysed. The O1s spectra deconvoluted into three peaks as shown in Fig. 2d, at around 529.1,

$$\text{Oxidation state} = \frac{[(\mathrm{IV}(\mathrm{SMn-O-Mn-SMn-OH})) + (\mathrm{III}(\mathrm{SMn-OH}))]}{\mathrm{SMn-O-Mn}} \tag{3}$$

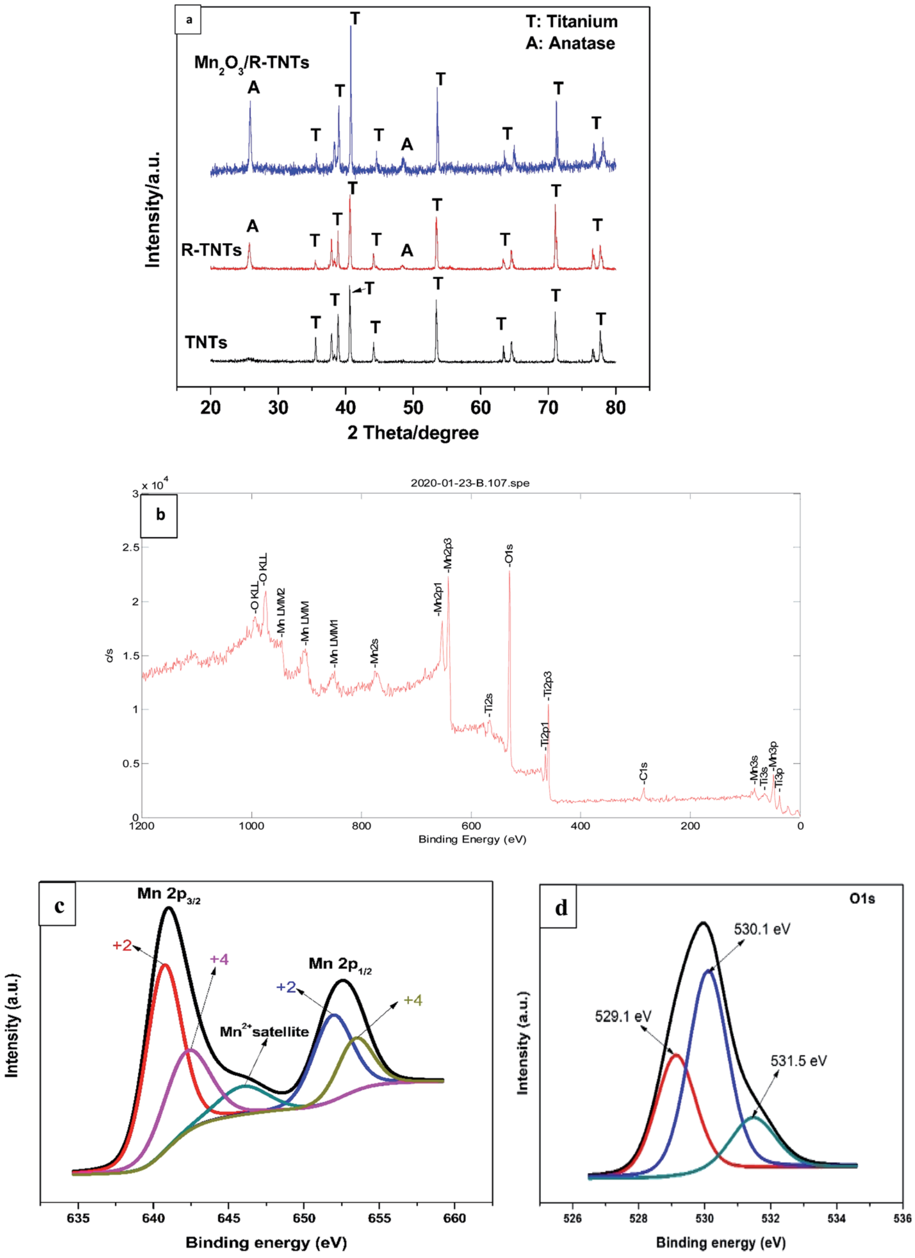

Fig. 2 (a) XRD pattern of TNTs, R-TNTs, and Mn_2O_3/R-TNTs. XPS spectra of Mn_2O_3/R-TNTs (b) survey spectra (c) Mn 2p and (d) O 1s spectra.

530.1 and 531.5 eV which can be attributed to Mn–O–Mn, Mn–OH, and H–O–H bonds signals, respectively.[32,39] The oxidation state of Mn can be determined from the intensities of Mn–O–Mn and Mn–OH signals by the following equation.[40]
where S is the bond corresponding to the signals from O 1s spectra. The average Mn oxidation state obtained from the equation is 2.99 (~3) for Mn_2O_3 nanoparticles. From this, the overall oxidation states of Mn are Mn^{2+}, Mn^{3+} and Mn^{4+}. The possible synthesis mechanisms of Mn_2O_3 by PED involved reduction and oxidation reactions during the V_{on} and V_{off}. In the first pulse cycle, Mn^{2+} is reduced when V_{on} is applied to the system, as below:

$$Mn^{2+} + 2e^{-} \rightarrow Mn \tag{4}$$

During V_{off}, the remaining Mn^{2+} in the solution is oxidized to Mn^{3+} and subsequently, the metastable Mn^{3+} is transformed into an intermediate MnOOH by hydrolysis. Consequently, MnOOH is oxidized to MnO_2.

$$Mn^{2+} \rightarrow Mn^{3+} + e^{-} \tag{5}$$

$$Mn^{3+} + 2H_2O \rightarrow MnOOH + 3H^{+} \tag{6}$$

$$MnOOH \rightarrow MnO_2 + H^{+} + e^{-} \tag{7}$$

As the pulse cycle continues, MnO_2 may be reduced to intermediate product MnOOH and further to MnO. But MnO is

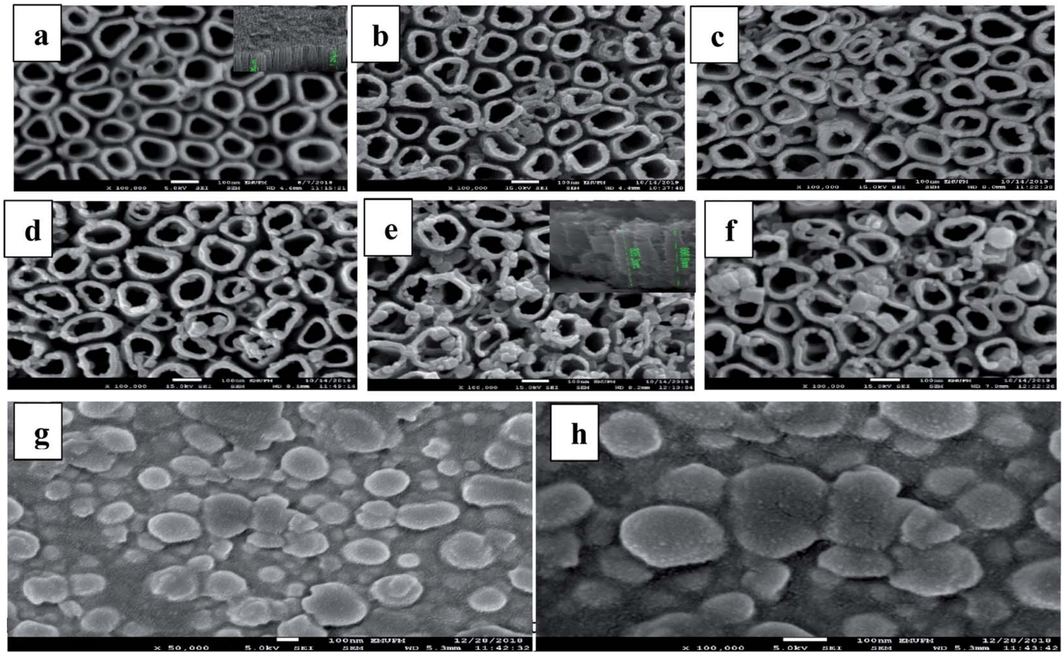

Fig. 3 Top view FESEM images of (a) R-TNTs and cross-sectional view (inset), and Mn_2O_3/R-TNTs electrodeposited at (b) 3 min, (c) 6 min, (d) 9 min, (e) 12 min (inset is cross-sectional view) and (f) 15 min. Mn_2O_3 deposited on Ti foil for 12 min (g) lower magnification, and (h) higher magnification.

unstable in the presence of oxygen and combine with MnO_2 to form Mn_2O_3.

$$MnO_2 + H^+ + e^- \rightarrow MnOOH \quad (8)$$

$$MnOOH + H^+ + e^- \rightarrow MnO + H_2O \quad (9)$$

$$MnO + MnO_2 \rightarrow Mn_2O_3 \quad (10)$$

Fig. 3a presents the FESEM images of R-TNTs with average inner diameter, wall thickness and tube length (inset) of 86 nm, 21 nm and 1.2 μm, respectively. Mn_2O_3 was successfully deposited onto the circumference as well as inside the R-TNTs for all the deposition times investigated as shown in Fig. 3b–f. The distinctive change in surface morphology before and after electrodeposition of Mn_2O_3 can be clearly observed. Obviously, as the deposition time increased the inner diameter of the nanotubes decreases while the wall thickness increases. The tube length become shorter after electrodeposition, for example at 12 min deposition time the average tube length is 850 nm. This may be due to the dense deposit of Mn_2O_3 formed on the nanotube circumference as the amount and size of Mn_2O_3 deposit increased with deposition time. For comparison, Mn_2O_3 was deposited on planar Ti for 12 min. As seen in Fig. 3g and h, the morphology and dimension of Mn_2O_3 is comparable to the one deposited on top of R-TNTs at 12 min deposition time even though the shape and structure of Mn_2O_3 deposits are more visible on the planar Ti. However, more uniform distribution of Mn_2O_3 deposits was obtained on R-TNTs as compared to Ti. This can be ascribed to the nanotubular structure of larger surface area that provides more nucleation sites than the Ti substrate. EDX analysis of Mn_2O_3/R-TNTs samples deposited at different times revealed the presence of four elements (Ti, O, C, Mn) in the Mn_2O_3/R-TNTs composite as confirmed by the XPS. The amount of each element in weight% is presented in Table 1.

The carbon present in the Mn_2O_3/R-TNTs sample is from the residual of glycerol used in anodization. The amount of Mn increases as the deposition time is increased as shown in Table 1. This is because of more pulse deposition cycles are applied as deposition time increases which leads to the increase in the amount of Mn deposits.

Electrochemical measurements

The electrochemical measurements of all the synthesised samples were conducted in 1 M KCl within the potential window of 0.0 to 0.8 V *vs.* Ag/AgCl. The CV profiles for R-TNTs recorded at different scan rates are displayed in Fig. 4a. It shows a symmetrical rectangular curves at all the scan rate measured and maintained the same shape even at high scan

Table 1 Elemental analysis for Mn_2O_3/R-TNTs as a function of deposition time

	Weight%			
Deposition time (min)	C	O	Ti	Mn
3	3.25	46.85	48.18	1.71
6	3.13	52.36	41.93	2.58
9	5.48	51.70	39.40	3.42
12	3.37	51.93	38.80	5.90
15	4.04	52.10	35.96	7.90

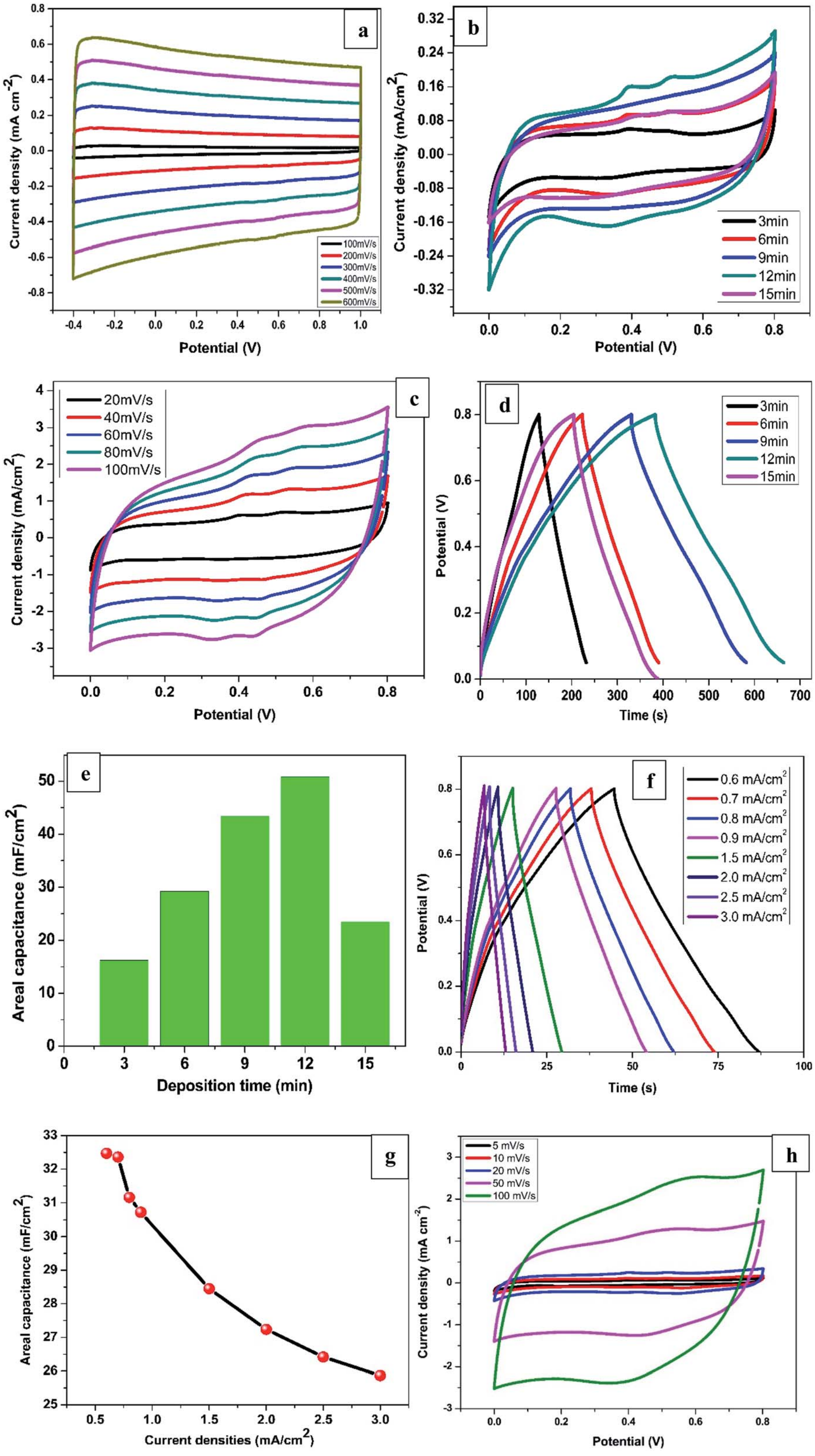

Fig. 4 CV curves of (a) R-TNTs at different scan rate, Mn_2O_3/R-TNTs (b) at different deposition time (c) as a function of scan rate for Mn_2O_3/R-TNTs synthesised for 12 min. (d) GCD curves of Mn_2O_3/R-TNTs at different deposition time. (e) Areal capacitance as a function of deposition time. (f) GCD curves of Mn_2O_3/R-TNTs synthesised for 12 min at different current densities, (g) areal capacitance as a function of current densities and (h) CV curves of Mn_2O_3/Ti at different scan rate.

rate of 600 mV s^{-1}. This is a typical characteristics of EDLC that exhibits excellent reversibility. The areal capacitance of R-TNTs evaluated at 100 mV s^{-1} is 3.82 mF cm^{-2}. The CV curves of Mn_2O_3/R-TNTs synthesised at different deposition time, measured at a scan rate of 5 mV s^{-1} are presented in Fig. 4b. All the cyclic voltammograms display near symmetrical rectangular shape, which is a typical of a mixture of EDLC and pseudocapacitive behaviour of the electrodes. The redox waves are obvious at 0.35, 0.40 and 0.52 V were due to the transition between Mn^{4+}/Mn^{2+} on the surface of the electrode.[26,37] The presence of both ions was confirmed by XPS. The Mn_2O_3/R-TNTs sample synthesised for 12 min shows higher integrated area and current response than the other samples which implies higher capacitive performance, therefore, was selected for further evaluation. CV at varying scan rates from 20 mV s^{-1} to 100 mV s^{-1} was performed as shown in Fig. 4c. The CV curves show an increased current density with the increase in scan rate, indicating the quasi-reversibility of the redox reactions and thus excellent capacitive behaviour. Even at high scan rate of 100 mV s^{-1} it still retains its shape and symmetry, indicating good ions diffusion into the electrode material from the electrolyte.

To further confirmed the capacitive performance of the samples, GCD measurement was performed at current density of 0.1 mA cm^{-2} as presented in Fig. 4d. All the GCD curves are linear and triangular suggesting good capacitive behaviour and coulombic efficiency. The sample synthesised for 12 min shows a longer discharging time indicating a higher capacitive performance which agrees with the result from the CV measurement. The areal capacitance as a function of deposition time is shown in Fig. 4e. The value increases from 16.2 mF cm^{-2} to 50.8 mF cm^{-2} as deposition time was increased from 3 min to 12 min due to the increase in mass loading of the Mn_2O_3 as confirmed by EDX. However, the areal capacitance for a sample synthesised for 15 min decreased by more than half (23.5 mF cm^{-2}) despite an increase in Mn_2O_3 mass loading. This can be ascribed to the increase in size of Mn deposits at 15 min deposition time which leads to partial coverage of nanotubes openings thereby reducing the electrolyte ions diffusion into the film.[13]

Fig. 4f displays the GCD curves of Mn_2O_3/R-TNTs synthesised for 12 min at different current densities. The GCD curves retained its shape even at high current density of 3.0 mA cm^{-2} with small IR drop (0.08 V) indicating excellent capacitive behaviour and good reversibility.[41]

Interestingly, the sample retained about 80% of the initial capacitance even at high current density of 3.0 mA cm^{-2} proving high-rate capability.[21,28] The areal capacitance as a function of current densities are depicted in Fig. 4g, the decrease in capacitance at higher current densities is as a result of inability of the electrolyte ions to fully accessed the electrode material.[15]

Fig. 4h displayed the CV curves at different scan rates for Mn_2O_3 deposited on planar Ti substrate for 12 min to further study the role of the nanotubes in electrochemical performance of the Mn_2O_3/R-TNTs composite. The areal capacitance of the sample measured at a scan rate of 5 mV s^{-1} is 35.51 mF cm^{-2} which is about 30% decrease in capacitance compared to the same sample deposited on R-TNTs. This indicates a superior capacitive

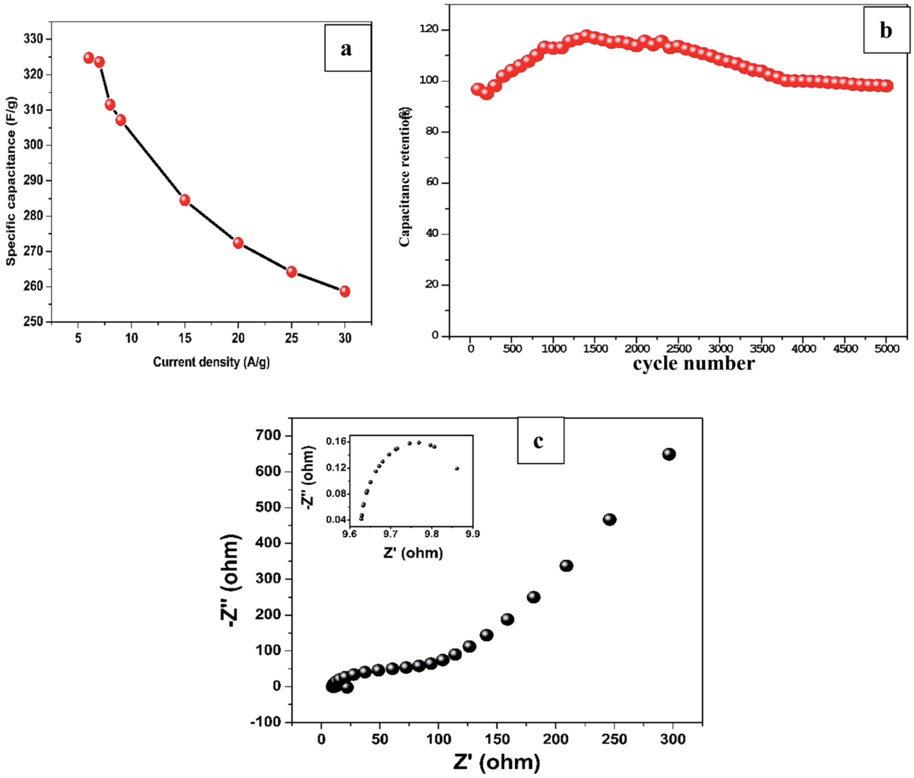

Fig. 5 (a) Specific capacitance of Mn_3O_4/R-TNTs-12 as a function of current density. (b) Cyclic stability of Mn_3O_4/R-TNTs-12 over 5000 cycles at 1 mA cm^{-2}. (c) Nyquist plot of Mn_3O_4/R-TNTs-12 with inset showing magnified high frequency region.

performance due to the nanotubular channels that enhanced diffusion of electrolytes ions to the current collector. Furthermore, the CV curve at higher scan rate of 100 mV s^{-1} for Mn_2O_3/Ti deviated slightly from rectangular compared to Mn_2O_3/R-TNTs sample measured at the same scan rate. This can be attributed to good reversibility of the sample due to the rapid electrons transfer across electrode/electrolytes interface as reported elsewhere.[16]

On the other hand, specific capacitance based on the mass of Mn_2O_3 obtained by average weight difference using analytical balance (0.1 mg accuracy) before and after electrodeposition for 12 min was evaluated at different current densities. The specific capacitance decreased from 324.7 F g^{-1} at 6 A g^{-1} to 258.7 F g^{-1} at 30 A g^{-1} as shown in Fig. 5a. The values are greater than most of the previously reported capacitances for Mn_xO_x for different composite materials as shown in Table 2.

Table 2 A comparison of electrochemical performance of various MnO_2 and its composites materials as electrode for supercapacitor

Material	Preparation method	Areal/specific capacitance	Current density/scan rate	Electrolyte	Capacitance retention	Ref.
Graphene/CNT/MnO_x	Dispersion & hydrothermal	210 F g^{-1}	Not mentioned	1 M Na_2SO_4	91% after 1000 cycles	2
MnO_2 nanoparticles	Precipitation method	250 F g^{-1}	1 mA cm^{-2}	1 M $Ca(NO_3)_2$	67% after 1000 cycles	17
Mn_3O_4 nanoparticles	Cathodic electrodeposition	416 F g^{-1}	1 A g^{-1}	1 M NaOH	47.1% after 1000 cycles	15
MnO_2/PEDOT	Anodic electrodeposition	159 F g^{-1}	5 mV s^{-1}	0.5 M Na_2SO_4	91% after 500 cycles	45
TiO_2@MnO_2	Hydrothermal	320 mF cm^{-2}	2 mA cm^{-2}	1 M Na_2SO_4	17.7% after 1000 cycles	18
MnO_2–TNTAs	Galvanostatic electrodeposition	40.4 mF cm^{-2}	0.032 mA cm^{-2}	0.1 M KOH	85.6% after 100 cycles	19
MnO_2–TiO_2	SCBD	175 mF cm^{-2}	10 mV s^{-1}	0.5 M Na_2SO_4	82.5% after 1000 cycles	16
MnO_2–TNTAs	Pulse current electrodeposition	425 F g^{-1}	0.5 A g^{-1}	0.5 M Na_2SO_4	71.4% after 3000 cycles	3
PPy/MnO_2	Cyclic voltammetry	596.3 F g^{-1}	0.5 A g^{-1}	0.5 M Na_2SO_4	87.6% after 1000 cycles	20
TiO_2@MnO_2	Hydrothermal	22.19 mF cm^{-2}	5 mV s^{-1}	1 M Na_2SO_4	85% after 4000 cycles	21
MnO_2/GA	Potentiostatic electrodeposition	410 F g^{-1}	2 mV s^{-1}	1 M Na_2SO_4	95% after 50 000 cycles	22
MnO_2 nanoparticles	Pulse current electrodeposition	290 F g^{-1}	5 mV s^{-1}	0.5 M Na_2SO_4	72% after 250 cycles	11
Mn_2O_3 nanoparticles	Pulsed laser deposition	210 F g^{-1}	1 mV s^{-1}	0.1 M Na_2SO_4	Not mentioned	46
MnO_2–TiO_2 NTs	SILAR	436.2 mF cm^{-2}	0.1 mA cm^{-2}	0.5 M Na_2SO_4	85.7% after 3000 cycles	5
MnO_2 microspheres	Solvothermal	190 F g^{-1}	0.5 A g^{-1}	1 M Na_2SO_4	∼100% after 1000 cycles	47
MnO_x/TiO_2/CFP	Galvanostatic electrodeposition	327 mF cm^{-2}	0.25 mA cm^{-2}	1 M Na_2SO_4	96% after 5000 cycles	23
MnO_2–TNT	Sono-chemical	65 mF cm^{-2}	1 mV s^{-1}	1 M KCl	95% after 2500 cycles	10
MnO_2/C	Dispersion	205 F g^{-1}	50 mV s^{-1}	2 M NaCl & 0.5 M TBAP/ACN	98% after 300 cycles	24
MnO_x–CDGs	Sonication & chemical reduction	280 F g^{-1}	1 A g^{-1}	1 M Na_2SO_4	94.7% after 10 000 cycles	48
MnO_2/AC	Grafting oxidation	332.6 F g^{-1}	2 mV s^{-1}	0.5 M Na_2SO_4	87% after 2000 cycles	25
CQDs/MnO_2	Sono-chemical	210 F g^{-1}	20 A g^{-1}	1 M Na_2SO_4	90.3% after 10 000 cycles	49
MnO_2 microspheres	Ultrasonic spray pyrolysis	320 F g^{-1}	2.5 mA cm^{-2}	1 M LiClO	98% after 1000 cycles	50
H–TiO_2/C/MnO_2	Hydrothermal	299.8 F g^{-1}	0.5 A g^{-1}	1 M Na_2SO_4	87% after 2000 cycles	8
Mn_2O_3/R-TNTs	Pulse reverse electrodeposition	18.32 mF cm^{-2}	0.1 mA cm^{-2}	1 M KCl	Not mentioned	13
MnO_x	Pulse current electrodeposition	252 F g^{-1}	10 mV s^{-1}	3 M KCl	Not mentioned	12
Mn_2O_3/R-TNTs	Pulse electrodeposition	324.72 F g^{-1}	6 A g^{-1}	1 M KCl	98% after 5000 cycles	Present work

To evaluate long-term cycling stability of the sample, GCD test was performed at 1 mA cm^{-2} which is ~10 A g^{-1} current density for 5000 cycles as shown in Fig. 5b. The GCD curves maintained its triangular shape even at 5000th cycle demonstrating excellent capacitive performance and superior reversibility. The sample retained 98% of the capacitance at the end of 5000 cycles after initial decrease to 95% at ~200th cycle which can be ascribed to the surface activation of the nanostructured material in the electrode induced by electrolyte ions penetration.[42,43]

EIS was conducted to explore the kinetic properties of Mn_2O_3/R-TNTs electrode as represented by a Nyquist plot in Fig. 5c. The intercept at real axis at high frequency region represents equivalent series resistance (ESR) which corresponds to the combination of bulk electrolyte resistance, contact resistance at the interface between current collector and active material and internal resistance of the active material. At mid frequency region, the diameter of the semicircle (shown as inset in Fig. 5c) represents the charge transfer resistance (R_{ct}) at the electroactive material/electrolyte interface, while the linear part at low frequency region corresponds to the combination of ion diffusion from electrolyte to the active material and accumulation of charges at the electrode surface.[20,44] The sample exhibits ESR and R_{ct} of 9.6 Ω and 0.4 Ω respectively, these considerably low resistance values indicate improved conductivity and charge storage capability of Mn_2O_3/R-TNTs sample.

Conclusion

A facile and cost-effective PED method was successfully used to deposit Mn_2O_3 nanoparticles onto R-TNTs at different deposition time to investigate the mass loading of Mn_2O_3 and its effect on the electrochemical performance of Mn_2O_3/R-TNTs. Mn_2O_3 nanoparticles have been uniformly deposited at the nanotubes circumference as shown by FESEM images which allowed for maximum utilization of the nanotubes surface area as pathway for ion diffusion across the current collector–electrolyte interface. The sample exhibited superior capacitive performance over the Mn_2O_3 deposited on planar Ti at the same deposition time. The mass loading and size of Mn_2O_3 deposits for Mn_2O_3/R-TNTs increased with increase in deposition time as revealed by EDX and FESEM analysis, respectively. However, the sample deposited for 12 min recorded the highest capacitance. CV and GCD measurement at different scan rates and current densities revealed pseudocapacitive characteristics, excellent rate capability and good reversibility of Mn_2O_3/R-TNTs and interestingly, a superior stability of 98% retention over 5000 long-term charging discharging cycles with considerably low ESR and R_{ct} values as deduced from EIS analysis. Therefore, these good electrochemical properties suggest that Mn_2O_3/R-TNTs composite can serve as a potential electrode for supercapacitor application.

Conflicts of interest

There are no conflicts to declare.

Acknowledgements

This research was funded by Putra Grant (UPM/700-2/1/GPB/2017/9555700). M.M.M acknowledges the sponsorship from Tertiary Education Trust Fund (TETFUND) and Gombe State University, Nigeria.

References

1 M. He, J. Li, W. Xu, Z. Dong, Y. Wu and L. Lv, *Nano*, 2019, **14**, 1–8.
2 M. A. A. Mohd Abdah, N. H. N. Azman, S. Kulandaivalu, N. Abdul Rahman, A. H. Abdullah and Y. Sulaiman, *J. Power Sources*, 2019, **444**, 227324.
3 H. Zhou, X. Zou and Y. Zhang, *Electrochim. Acta*, 2016, **192**, 259–267.
4 J. Li, X. Wang, X. Yu, C. Ma and J. Zhao, *Int. J. Hydrogen Energy*, 2016, **41**, 22162–22170.
5 Z. Li, X. Wang, X. Wang, T. Xiao, L. Zhang, P. Lv and J. Zhao, *Int. J. Hydrogen Energy*, 2018, **43**, 8859–8867.
6 M. Salari, K. Konstantinov and H. K. Liu, *J. Mater. Chem.*, 2011, **21**, 5128–5133.
7 M. Salari, S. H. Aboutalebi, A. T. Chidembo, I. P. Nevirkovets, K. Konstantinov and H. K. Liu, *Phys. Chem. Chem. Phys.*, 2012, **14**, 4770–4779.
8 J. Di, X. Fu, H. Zheng and Y. Jia, *J. Nanopart. Res.*, 2015, **17**, 255, DOI: 10.1007/s11051-015-3060-z.
9 N. A. Samsudin, Z. Zainal, H. N. Lim, Y. Sulaiman, S. K. Chang, Y. C. Lim and W. N. Mohd Amin, *J. Nanomater.*, 2018, 9509126, DOI: 10.1155/2018/9509126.
10 H. R. Barai, A. N. Banerjee, F. Bai and S. W. Joo, *J. Ind. Eng. Chem.*, 2018, **62**, 409–417.
11 H. Adelkhani and M. Ghaemi, *J. Alloys Compd.*, 2010, **493**, 175–178.
12 F. Xiao and Y. Xu, *Int. J. Electrochem. Sci.*, 2012, **7**, 7440–7450.
13 N. A. Samsudin, Z. Zainal, H. N. Lim, Y. Sulaiman, S. K. Chang, Y. C. Lim, A. K. Ayal and W. N. Mohd Amin, *RSC Adv.*, 2018, **8**, 23040–23047.
14 H. A. El-Fattah, I. El-Mahallawi, M. Shazly and W. Khalifa, in *Energy Technology, the Minerals, Metals & Materials Series*, ed. T. Wang, *et al.*, Springer, 2019, part III, pp. 253–263, DOI: DOI: 10.1007/978-3-030-06209-5_2.
15 T. Nguyen, M. João Carmezim, M. Boudard and M. Fátima Montemor, *Int. J. Hydrogen Energy*, 2015, **40**, 16355–16364.
16 H. Zhou and Y. Zhang, *J. Power Sources*, 2014, **272**, 866–879.
17 R. Aswathy, Y. Munaiah and P. Ragupathy, *J. Electrochem. Soc.*, 2016, **163**, A1460–A1468.
18 X. Y. Liu, M. Zhou, C. Chen and Y. X. Zhang, *Ceram. Int.*, 2017, **43**, 10595–10600.
19 Y. Huang, X. Zhang, Xi. Chen, H. Wang, J. Chen, X. Zhong and Q. Li, *Int. J. Hydrogen Energy*, 2015, **40**, 14331–14337.
20 M. He, Y. Zheng and Q. Du, *Nano*, 2013, **8**, 1–7.
21 A. Ramadoss and S. J. Kim, *Int. J. Hydrogen Energy*, 2014, **39**, 12201–12212.
22 C. C. Wang, H. C. Chen and S. Y. Lu, *Chem.–Eur. J.*, 2014, **20**, 517–523.

23 L. Li, X. Zhang, G. Wu, X. Peng, K. Huo and P. K. Chu, *Adv. Mater. Interfaces*, 2015, **2**, 1–10.

24 V. M. Tran, A. T. Ha and M. L. P. Le, *Adv. Nat. Sci.: Nanosci. Nanotechnol.*, 2014, **5**, 025005, DOI: 10.1088/2043-6262/5/2/025005.

25 J. W. Wang, Y. Chen and B. Z. Chen, *J. Electrochem. Soc.*, 2015, **162**, A1654–A1661.

26 M. Krajewski, P. Y. Liao, M. Michalska, M. Tokarczyk and J. Y. Lin, *J. Energy Storage*, 2019, **26**, 101020.

27 A. Y. Lo, L. Saravanan, C. M. Tseng, F. K. Wang and J. T. Huang, *ACS Omega*, 2020, **5**, 578–587.

28 I. I. Gurten Inal and Z. Aktas, *Appl. Surf. Sci.*, 2020, **514**, 145895.

29 M. Hakamada, A. Moriguchi and M. Mabuchi, *J. Power Sources*, 2014, **245**, 324–330.

30 M. Elrouby, A. M. Abdel-Mawgoud and R. A. El-Rahman, *J. Mol. Struct.*, 2017, **1147**, 84–95.

31 M. H. Pham, A. Khazaeli, G. Godbille-Cardona, F. Truica-Marasescu, B. Peppley and D. P. J. Barz, *J. Energy Storage*, 2020, **28**, 101210.

32 W. Cong, R. Miao, F. Miao and B. Tao, *Mater. Res. Express*, 2017, **40**, 245–257.

33 A. Moses Ezhil Raj, S. G. Victoria, V. B. Jothy, C. Ravidhas, J. Wollschläger, M. Suendorf, M. Neumann, M. Jayachandran and C. Sanjeeviraja, *Appl. Surf. Sci.*, 2010, **256**, 2920–2926.

34 D. Wang, Y. Li, Q. Wang and T. Wang, *Eur. J. Inorg. Chem.*, 2012, 628–635.

35 G. An, P. Yu, M. Xiao, Z. Liu, Z. Miao, K. Ding and L. Mao, *Nanotechnology*, 2008, **19**, 275709, DOI: 10.1088/0957-4484/19/27/275709.

36 J. Zhang, Y. Wang, Y. Qin, C. Yu, L. Cui, X. Shu, J. Cui, H. Zheng, Y. Zhang and Y. Wu, *J. Solid State Chem.*, 2017, **246**, 269–277.

37 Y. Xu, L. Wang, Y. Zhou, J. Guo, S. Zhang and Y. Lu, *J. Electroanal. Chem.*, 2019, **852**, 113507.

38 J. Xu, K. Hou, Z. Ju, C. Ma, W. Wang, C. Wang, J. Cao and Z. Chen, *J. Electrochem. Soc.*, 2017, **164**, A430–A437.

39 R. Tholkappiyan, A. N. Naveen, K. Vishista and F. Hamed, *J. Taibah Univ. Sci.*, 2018, **12**, 669–677.

40 S. Yang, K. Cheng, J. Huang, K. Ye, Y. Xu, D. Cao and X. Z. G. Wang, *Electrochim. Acta*, 2014, **120**, 416–422.

41 N. Ain, M. Amirul, A. Mohd, N. Hawa, N. Azman and Y. Sulaiman, *J. Electroanal. Chem.*, 2020, **867**, 114188.

42 A. E. Elkholy, F. E. Heakal and N. K. Allam, *RSC Adv.*, 2017, **7**, 51888–51895.

43 W. Teng, X. Wang, T. Wang, L. Su, T. Tesfamichael and F. Yu, *J. Alloys Compd.*, 2019, **803**, 950–957.

44 M. P. Clark, W. Qu and D. G. Ivey, *ECS Trans.*, 2015, **64**, 57–67.

45 T. A. Ha, V. M. Tran and M. L. P. Le, *Adv. Nat. Sci.: Nanosci. Nanotechnol.*, 2013, **4**, 035004, DOI: 10.1088/2043-6262/4/3/035004.

46 D. Yang, *J. Power Sources*, 2013, **228**, 89–96.

47 W. Y. Ko, L. J. Chen, Y. H. Chen and K. J. Lin, *J. Mater. Res.*, 2014, **29**, 107–114.

48 B. Unnikrishnan, C. W. Wu, I. W. P. Chen, H. T. Chang, C. H. Lin and C. C. Huang, *ACS Sustainable Chem. Eng.*, 2016, **4**, 3008–3016.

49 R. Thangappan, M. Arivanandhan, R. Dhinesh Kumar and R. Jayavel, *J. Phys. Chem. Solids*, 2018, **121**, 339–349.

50 Y. Zhang, L. A. Huff, A. A. Gewirth and K. S. Suslick, *Part. Part. Syst. Charact.*, 2015, **32**, 899–906.